Re-entry survival analysis and ground risk assessment of space debris considering by-products generation

Seong-Hyeon Park [a], Javier Navarro Laboulais [b], Pénélope Leyland [a], Stefano Mischler [a,*]

[a] *Ecole Polytechnique Fédérale de Lausanne EPFL, Tribology and Interface Chemistry Group (SCI-STI-SM), Station 12, Lausanne, CH-1015, Switzerland*
[b] *Chemical and Nuclear Engineering Department, Universitat Politècnica de València UPV, Valencia, Spain*

ARTICLE INFO

ABSTRACT

Space debris that re-enter the Earth's atmosphere can be partially or fully ablated along the trajectory path after hitting the atmosphere layers, once these become denser (approximately below 82 km). This paper combines re-entry survival analysis to by-product generation analyses according to specific trajectory analysis and different levels of modelling within the re-entry simulation tool. Particular attention is made on metallic alloy decomposition and metallic oxides formation from the debris' materials ablation. Generic alloys present within satellite constructions are considered. The flow field in the induced shock layer is considered to be in non-equilibrium and the trajectory tool is based on a 3DOF object-oriented approach. The by-product analyses give important information on emitted species in the atmosphere at different altitudes, and the risk of substances reaching the ground is evaluated as a function of the initial break-up altitude. The non-equilibrium atmospheric chemistry within the shock layer has a significant impact for the re-entry analysis.

1. Introduction

In recent years, Space Situational Awareness (SSA) on man-made space debris has become an important global issue. In the Low Earth Orbit (LEO), the majority of space debris have high kinetic energy and they are a serious threat to orbiting objects such as satellites and space stations. In addition, the lifetime of the orbiting objects in the LEO is limited due to perturbations such as solar radiation pressure and atmospheric drag, and they eventually re-enter the Earth's atmosphere [1]. Although most of them are completely burned up when impacting the atmosphere, some surviving objects can cause risks to the human population and properties on the ground [1,2]. Moreover, the thermal degradation of the surface of the debris' materials can generate chemical by-products that may potentially contribute to atmosphere pollution and trigger adverse chemical reactions for instance for the ozone layer. Predicting the degree of degradation of space debris is therefore of great concern for space agencies such as ESA and NASA in order to mitigate the ground risks and environmental problems.

Regarding these concerns, re-entry analysis tools have been developed and improved to predict the trajectory and survivability of re-entry objects. The most representative tools include SCARAB, ORSAT, DRAMA/SESAM, and DEBRISK [2–7]. They can be mainly classified in two categories: spacecraft-oriented and object-oriented. The spacecraft-oriented tools simulate spacecraft re-entry using a detailed modelling as close to the actual spacecraft as possible. Although the results can represent a detailed assessment, they require a modelling complexity and computational burden. These tools are of great importance, but cannot be perceived to function in real-time simulation when an actual spacecraft debris is hitting the Earth's atmosphere. In contrast, the object-oriented tools use relatively simpler models of a spacecraft and its components, which simplifies the computation process, allowing users to run fast and extensive parametric and statistical analyses [6, 8–10]. Most of the existing tools, as the examples listed here, except SCARAB, are examples of object-oriented tools. In reality, it is difficult to predict the exact re-entry orbital elements. Therefore, in case of unexpected and/or uncontrolled re-entry, the initial conditions need to be updated and applied to the simulations in real time for the accurate analysis.

Re-entry problems are complex and there are a lot of uncertainties including ablation, non-equilibrium surface heat transfer, as well as break-up/fragmentation [9,11]. To date, the uncertainties have not been fully understood in the existing tools and in particular the impact of implementation of the non-equilibrium flow approaches to the re-entry analysis tool has not been conducted nor documented. The impact of considering non-equilibrium heat transfer levels presented in this paper

---

Nomenclature

A	area, $[m^2]$
c	atomic mass fraction, $[-]$
c_d	drag coefficient, $[kg/m^2]$
C_p	specific heat, $[J/kg\text{-}K]$
e	internal energy, $[J/kg]$
E	total energy, $[J/kg]$
G	total Gibbs free energy, $[J]$
h	enthalpy, $[J/kg]$
h_f	heat of fusion, $[J/kg]$
h_R	heat of recombination, $[J/kg]$
k	thermal conductivity, $[W/m\text{-}K]$
k_B	Boltzmann constant, $[J/K]$
k_w	catalytic velocity, $[m/s]$
Kn	Knudsen number, $[-]$
$M_i(z)$	accumulated emitted mass of the i-th by-product $[kg]$
m	atomic mass, $[kg]$
n_i	mole number of component i, $[mol]$
N	number of species, $[-]$
p	pressure, $[Pa]$
Pr	Prandtl number, $[-]$
q	heat flux, $[W/m^2]$
R	gas constant, $[J/K\text{-}mol]$
Sc	Schmidt number, $[-]$
t	time, $[s]$
T	temperature, $[K]$
u	velocity, $[m/s]$
w_i	mass fraction of component i, $[-]$
x_i	molar fraction of component i, $[-]$
z	altitude, $[m]$

Greek Letters

β	velocity gradient, $[1/s]$
ε	material emissivity, $[-]$
γ	catalytic recombination coefficient, $[-]$
μ	viscosity, $[kg/m\text{-}s]$
μ_i	chemical potential of component i, $[J/mol]$
$\dot{\Omega}_{EC}$	electron-chemistry energy exchange source term, $[W/m^3]$
$\dot{\Omega}_{ET}$	electron-translation energy exchange source term, $[W/m^3]$
$\dot{\Omega}_{VC}$	vibration-chemistry energy exchange source term, $[W/m^3]$
$\dot{\Omega}_{VT}$	vibration-translation energy exchange source term, $[W/m^3]$
$\dot{\omega}$	mass production source term, $[kg/m^3\text{-}s]$
ρ	density, $[kg/m^3]$
σ	Stephan-Boltzmann constant, $[W/m^2\text{-}K^4]$
ϕ	catalytic factor, $[-]$

Subscript

c	conductive
C	condensed
d	diffusive
e	free-electrons
g	gas
rad	radiation
rr	re-radiation
s	chemical species
se	stagnation at boundary layer edge
st	stagnation-point
SRF	surface
STD	standard atmosphere
ve	vibration-electron-electronic thermal energy mode
w	wall

is strongly related to the re-entry survivability and the thermal break-up. During re-entry of space debris through the atmosphere, extremely high velocities are encountered, and detached/attached shocks are formed in front of the debris entities dependent on their respective geometrical shapes and their respective attitudes. In the case of blunt body shapes, a clear bow shock is formed. Across the shock wave, most of the free-stream kinetic energy is transformed into thermal energy, causing excited molecular vibration, dissociation, and ionisation within the shock layer. Also, the flow becomes subsonic in the near wall stagnation region. Dependent on the instantaneous attitude of the debris geometries, the shock layer can be sufficiently developed that the flow can re-accelerate to the body and some recombination of oxygen and/or nitrogen may take place [12,13].

There are two limiting cases: frozen flow and equilibrium flow. In the first case, the internal energy modes and the chemical composition of the gas flowing along a streamline can maintain their local equilibrium values, that is, they have infinitely fast reaction rates or a zero relaxation time. In the other case, the gas moves so fast that the internal energy modes have no time to follow the changing density and temperature with the nearly constant energies in vibration, dissociation, and ionisation [14]. Depending on the free-stream conditions, air compositions, and the size of the body, the flow may be either almost frozen or nearly equilibrium. It is known that most of the aforementioned re-entry analysis tools calculate the stagnation-point heat transfer using correlations such as the well known Lees' and Fay and Riddells' formulae which assume an equilibrium flow with fully catalytic wall condition [2, 11,15]. However, the equilibrium flow which has infinitely fast reaction rates can underestimate the flow temperature as well as overestimate dissociated atoms in the shock layer. At hypersonic velocities, especially for the small objects, the time available is generally too short for the particles which are experiencing rapid temperature, density, and

chemical composition changes to reach thermodynamic equilibrium. Hence, a thermal and chemical non-equilibrium situation usually exists in the shock layer [12].

The objective of the present study, is firstly to investigate the effect of taking into account non-equilibrium flow conditions on the re-entry survivability and ground risk estimation, and secondly to consider the associated by-products released at the surface, which can migrate through the shock layer and be presented within the environment of the debris in the atmosphere. Indeed, the high temperature non-equilibrium flow in the shock layer and the ablation phenomena that occur at the surface of the re-entry object incur the emission at the surface of by-products depending on the debris' material composition. This can include a variety of metallic by-products (such as the metallic oxides Al_2O_3, TiO_2, etc.) with their interaction with the atmosphere, and by-products from graphite epoxies, polymeric compounds (with and without carbon fibres), glasses, and battery disintegration [16]. Also, independently of the air dissociation in the shock-layer, NO_x can be produced which may cause supplementary atmospheric pollution. Moreover, the generated by-products interact with the near wall gas condition in-between the boundary layer and the surface of the object, and the chemical reactions may change the net heat transfer on the surface. The outcomes of the study help characterise the eventual atmospheric pollution by satellite debris re-entry and the impact of a higher order modelling on the ground risk evaluations. In the first part of this paper the impact of taking into account non-equilibrium chemistry conditions in object-orientated approaches is evaluated. In the second part, by-products generation are investigated using an in-house kinetic evaluation. Finally, the ground risk assessment is conducted considering thermal break-up. The discussion of the results completes the paper.

2. Re-entry analysis

In this study, the object-oriented re-entry analysis tool has been used to assess the re-entry survivability and on-ground risk of space debris. One of the main features of this type of tool is the fast simulation that enables users to do extensive parametric and statistical analyses using primitive shapes such as spheres, cylinders, boxes, and flat plates. The re-entry tool integrates trajectory, atmosphere, aerodynamics, aerothermodynamics, thermal analysis, ablation, and break-up modules. This tool was first developed in a previous study and its results were compared and validated with existing tools based on the same initial conditions [1,11]. This tool (which is called 'ATD Trajectory Tool (ATDTT)' in this study) is continuously being improved in order to interpret various re-entry scenarios. Fig. 1 depicts a diagramme of the modules used in the re-entry analysis tool.

The trajectory module is a three-degrees-of-freedom (3-DOF) flight dynamics that describes the propagation of the trajectory considering the object as a point mass. The equations derived in an Earth-fixed reference frame assuming a rotating Earth sphere are used and solved using a fourth order Runge-Kutta numerical integration scheme. The aerodynamic and gravitational forces are considered. Several atmosphere models are available in this tool including the 1976 U.S. Standard Atmosphere and NRLMSISE00 models. The 1976 U.S. Standard Atmosphere with a two-harmonics gravity model is mainly used and the atmospheric temperature, density, and pressure depending on the altitude are provided. The aerodynamics module calculates average aerodynamic coefficients of objects for free molecular, transitional, and continuum flow regimes as a function of the Knudsen number (Kn) which is the ratio of the mean-free path in the atmosphere and the size of the object (characteristic length) [17,18]. The aerodynamic coefficients in the continuum flow and free-molecular flow regimes are commonly computed using the modified Newtonian flow theory and the Schaaf-Chambre method, respectively. In the transitional flow ($0.01 < Kn < 10$), they are computed based on a bridging function between free molecular and continuum flow regimes [8–10,19,20].

The net heat flux to the re-entry object is calculated in the aerothermodynamics module. The net heat flux is sum of both the hot wall convective heat flux and the oxidation heat flux and subtracting the wall re-radiation heat flux, see Eqs. (9)–(12), (14). The hot wall convective heat flux is computed as the cold wall convective heat flux multiplied by the wall enthalpy ratio [15]. The cold wall convective heat flux is calculated using averaging factors, which provide the relationship between a stagnation-point heat flux and the average heat flux on the object as a function of its geometrical shape and the attitude motion of the object [21]. To calculate the stagnation-point heat flux, a relationship consisting of the freestream density, the freestream velocity, and the free molecular thermal accommodation is used in the free molecular flow [11]. The variation of Stanton number is used based on a bridging formula between the free-molecular and continuum flow regimes for the transitional flow [17]. The stagnation-point heat flux calculation

considering thermodynamic non-equilibrium for the continuum flow will be discussed later. The oxidation heat flux is commonly obtained by multiplication of the net oxygen atom mass flux to the wall by the heat of oxidation. The re-radiation heat loss is computed using the Stephan–Boltzmann equation with the temperature of the outer surface and the thermal emissivity, see Eq. (14)

The surface temperature and inner temperature of the object are provided by the thermal analysis module. As the amount of absorbed heat from the outside increases during re-entry, the surface and inner temperatures increase by heat conduction. The rapid temperature change of the object can be accurately predicted by an unsteady heat conduction which considers the change in the energy capacity with the time of the volume element. By assuming the same energy capacity change of the volume element over time $\triangle t$, the temperature change for each node is predicted by the amount of heat transferred from the surface [22]. In this module, a nodal thermal math model is used, and the differential equation for the 1-D thermal mathematical model is solved using a Forward Time Central Space (FTCS) finite difference scheme [23]. The FTCS scheme is a first order method in time, and it is given in the form of a second order derivative in Eq. (1):

$$\frac{\partial^2 T}{\partial x^2} = \frac{1}{\alpha}\frac{\partial T}{\partial t} \tag{1}$$

For a spinning sphere, the differential equation can be given in spherical coordinates as,

$$\rho C_p \frac{\partial T}{\partial t} = \frac{1}{r^2}\frac{\partial}{\partial r}\left(kr^2\frac{\partial T}{\partial r}\right) \tag{2}$$

where r is the distance in radial direction. For each interior node, the temperature is calculated using the following finite difference relationships for the absorbed/emitted heat (Q), Eq. (3)

$$Q_{in} - Q_{out} = kA\frac{T_{j+1,i}-T_{j,i}}{\triangle x} - kA\frac{T_{j,i}-T_{j-1,i}}{\triangle x}$$
$$= \rho A\triangle x C_p\frac{T_{j,i+1}-T_{j,i}}{\triangle t} \tag{3}$$

$$T_{j,i+1} = \tau\left(T_{j-1,i}+T_{j,i}\right) + (1-2\tau)T_{j,i} \tag{4}$$

$$\tau = \frac{\alpha\triangle t}{\triangle x^2} \le \frac{1}{2} \tag{5}$$

where the subscripts j and i denote node index and time index, respectively. α is the thermal diffusivity ($K/\rho C_p$) and τ is the dimensionless mesh Fourier number [11,22,24].

The ablation module determines whether the outer layer of an object is removed or not. After the temperature of the outer layer reaches the melting temperature of the material, the temperature is fixed and the heat load of each layer with respect to time is tracked by the thermal analysis module. When the temperature of the node exceeds the melting temperature and the absorbed heat exceeds the heat of ablation of that
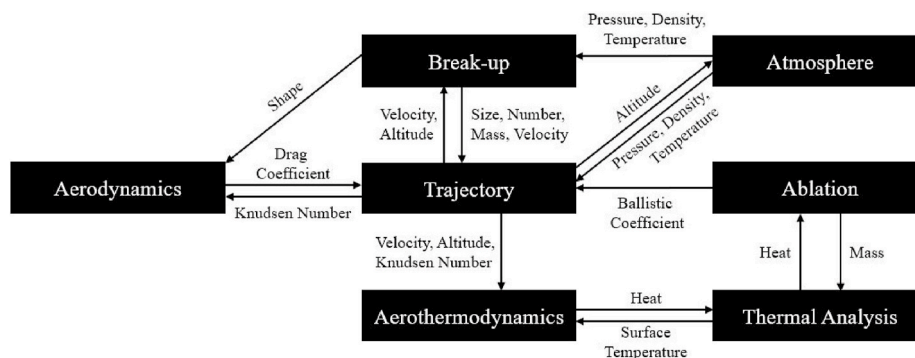

Fig. 1. Schematic diagram of the re-entry ATD Trajectory Tool (ATDTT).

layer, the layer is eliminated by an assumed shear force and the net heat flux is applied to the next layer. The ablation can be expressed as,

$$\frac{dm}{dt} = -\frac{\dot{Q}}{h_f} = -\frac{A_w}{h_f}\left[\dot{q}_{st} - \varepsilon\sigma T_w^4\right] \tag{6}$$

where h_f is the heat of fusion of the material. The ablated mass according to the re-entry trajectory (dm/dz) can also be estimated based on Eq. (6). The material database used for the ATDTT is obtained from the NASA Debris Assessment Software 3.0 (DAS 3.0) [25]. As a result, the changed mass, size, and ballistic coefficient of the object are applied to the other modules. The process continues until all layers are melted or the object reaches the ground [15].

The break-up module is included in this tool. Particularly, the experimental data for the separation process are considered from the previous work [26]. This module can provide the break-up altitude, time, and the characteristics of fragments (number, size, and shape). After the break-up occurs, the object is fragmented and each fragment having different ballistic coefficient is separated with lateral velocity induced by shock-shock interaction. The information is then applied to the trajectory and aerodynamics modules, and the process runs again.

3. Hypersonic non-equilibrium aerothermodynamics

3.1. Post shock relaxation

The post shock conditions were numerically calculated using the Poshax3, which is a well-known code developed at the University of Queensland [27,28]. The code is an extension of the Post-SHock relAXation solver (Poshax) code originally developed by Gollan to two- and three-temperature gases with fully coupled governing equations. It solves for the spatial variation in flow properties behind a strong shock assuming inviscid and one-dimensional flow. Source terms due to chemical reactions, thermal energy exchange and radiative cooling are able to be considered. The post shock relaxation equations can be derived from the full Navier-Stokes equations, and the following equations for a two temperature gas are therefore solved.

$$\frac{\partial\rho_s}{\partial t} + \frac{\partial}{\partial x}(\rho_s u) = \dot{\omega}_s$$

$$\frac{\partial\rho u}{\partial t} + \frac{\partial}{\partial x}(\rho u^2 + p) = 0$$

$$\frac{\partial\rho E}{\partial t} + \frac{\partial}{\partial x}(u(\rho E + p)) = -\frac{\partial q_{rad}}{\partial x} \tag{7}$$

$$\frac{\partial\rho e_{ve}}{\partial t} + \frac{\partial}{\partial x}(u(\rho e_{ve} + p_e)) = -\frac{\partial q_{rad}}{\partial x} + \dot{\Omega}_{VT} + \dot{\Omega}_{ET} + \dot{\Omega}_{VC} + \dot{\Omega}_{EC}$$

where the upper dot denotes differentiation with respect to time. Eq. (7) represents the conservation equations for species mass, momentum total energy, and vibration-electron-electronic energy. For a three temperature model in the steady flow, the vibration and electron-electronic energy continuity equations can be expressed as follows [28], Eq. (8)

$$\frac{\partial}{\partial x}(ue_v) = \dot{\Omega}_{VT} + \dot{\Omega}_{VE} + \dot{\Omega}_{VC}$$

$$\frac{\partial}{\partial x}(u(e_e + p_e)) = -\frac{\partial q_{rad}}{\partial x} + \dot{\Omega}_{ET} + \dot{\Omega}_{EV} + \dot{\Omega}_{EC} \tag{8}$$

Detailed description can be found in Refs. [27,28]. In the present work, the spatial step Δx was set to $10^{-5}m$ and a three temperature 11 species (O, N, O_2, N_2, NO, O^+, N^+, O_2^+, N_2^+, NO^+, e^-) air model was mainly considered with transrotational, vibrational, and electronic thermal modes. The used chemical reaction rate coefficients are discussed in Ref. [28]. The chemical-kinetic and vibration-transition energy exchange model by Park [29] was implemented, with the translation-electron energy exchange model of Gnoffo [30]. The viscosity of an ionised gas-mixture was obtained by the Gupta-Yos's

mixture rule [31]. To calculate the shock stand-off distance, the theory of Serbin was used considering the frozen density ratio across the shock wave [32,33]. The freestream conditions were determined according to the re-entry trajectory with a air composition of 78% of N_2 and 22% of O_2.

3.2. Heat transfer theory

In the heat flux calculation, Goulard's heat transfer theory was used considering wall catalytic recombination. With Goulard's theory, the flow was assumed to be in a state of chemically frozen in the boundary layer. In the formulation, the heat transfer consists of two main parts: conductive heat transfer (q_c) which is manifested by the temperature gradient, and diffusive heat transfer (q_d) which is from catalytic recombination at the wall. The stagnation-point heat transfer, based on the binary gas mixture, is expressed as [34],

$$q_{st} = q_c + q_d \tag{9}$$

$$q_c = 0.47(2\beta\mu_{se}\rho_{se})^{1/2}\overline{Pr_w}^{-2/3}\overline{h}_{se} \tag{10}$$

$$q_d = 0.47(2\beta\mu_{se}\rho_{se})^{1/2}Sc^{-2/3}h_R c_{se}\phi \tag{11}$$

$$\phi = \frac{1}{1 + \frac{0.47Sc^{-2/3}(2\beta\mu_{se}\rho_{se})^{1/2}}{\rho_w k_w}} \tag{12}$$

where β is the stagnation-point velocity gradient (β $= du_e/dx$, where u_e is the velocity at boundary layer edge and x is the distance along the wall from the stagnation-point). Sc was assumed to be 0.485 to follow the binary gas assumption. μ_{se} was calculated using a Wilke's mixture-rule based on temperature and the species composition of the gas mixture [30]. ϕ represents the catalytic effect in the heat transfer formulation through the catalytic velocity k_w. The catalytic velocity depending on the catalytic recombination probability can be expressed as,

$$k_w = \frac{\gamma_w}{4}\sqrt{\frac{8k_B T_w}{\pi m}} \tag{13}$$

γ_w is the wall catalytic efficiency defined as the ratio of the number of atoms recombining on a surface per unit area and time to the total number of atoms striking the surface per unit area and time. Assuming the Chapman-Rubesin constant of unity ($\rho_w\mu_w/\rho_{se}\mu_{se}$) after Goulard, the density at the wall (ρ_w) was determined.

The re-radiation heat loss was obtained using the Stephan-Boltzmann equation with the emissivity and the surface temperature of the object. It can be expressed as follows,

$$q_{rr} = \varepsilon\sigma T_w^4 \tag{14}$$

where σ is the Stephan-Boltzmann constant (5.67×10^{-8} W/m^2-K^4) [11]. The oxidation heat flux calculation was not included in this work.

4. By-products generation

The re-entry of space debris such as satellites or rocket-body parts can lead to the formation of different chemical by-products depending of the original composition of the objects in contact with the air in the upper atmosphere. The original kinetic energy of the air around the objects is converted into heat increasing the surface temperature, and then favouring the oxidation (burning) of its complex components. Knowing the pressure and temperature conditions under hypersonic flow, allows the thermodynamic determination of the most chemically stable by-products. The method developed here to quantify these by-products is based on Gibbs Energy Minimisation (GEM), i.e. the determination of the chemical composition in a complex mixture for a closed system at given pressure P and temperature T, minimising the Gibbs free

energy of all the possible chemical species [35–40]. The output of the trajectory-analysis programme described above, Fig. 1, estimates the ablated masses of the spacecraft components and the surface temperatures. Assuming the pressure profile of the Standard Atmosphere along the re-entry trajectory and that the atmosphere composition of N_2 = 79% and O_2 = 21% constant below 100 km, and knowing the chemical composition of the ablating materials, the by-products composition emitted to the atmosphere can be determined by GEM.

The minimisation of the Gibbs free energy is subject to the atomic molar balance. In fact, the composition is evaluated solving the problem:

$$\min G(P,T,n) = \sum_N n_i \cdot \mu_i(P,T,n) \tag{15}$$

subject to constraint,

$$A\,n = b \tag{16}$$

with

$$n \geq 0 \tag{17}$$

where A is the atomic matrix relating the chemical species with atomic composition and b is the element abundance vector. Since the chemical potential is also a function of the chemical composition, the problem is reduced to the calculation of the n_i minimising the Gibbs energy.

The chemical potential for ideal systems can be expressed directly in terms of molar compositions; however, for real systems, the chemical potential should be expressed in terms of fugacity (gases) or activities (condensed phases). Because the atmosphere pressure is low enough at the reentry, we can assume ideal conditions for the gas phase. Moreover, if pure solids are produced during the material ablation, the activities of these substances can be assumed the unity. Then, for convenience in our problem, we split Eq. (15) as:

$$\min G(P,T,n) = \sum_{N_c} n_i \cdot \mu_i(T,N_c) + \sum_{N_g} n_j \cdot \mu_j(P,T,N_g) \tag{18}$$

The chemical potential for the gas and the condensed species can be expressed as:

$$\mu_i(T,N_c) = \mu_i^*(T)$$

$$\mu_j(P,T,N_g) = \mu_j^*(T) + RT\ln\left(\frac{n_j}{\sum_{N_g} n_j}\right) + RT\ln\left(\frac{P}{P^*}\right) \tag{19}$$

where $\mu_i^*(T)$ and $\mu_j^*(T)$ are the standard chemical potentials or conversely, the chemical potential in the standard state, and P^o is the pressure of reference at ground level (1 bar).

The general procedure for the calculation of the by-products profiles along the re-entry trajectory is summarised in Fig. 2. The aerothermodynamic trajectory code provides the surface temperature, the trajectory path of the spacecraft and the thermochemical state of the atmosphere along the trajectory. The solution of Eqs. (15)–(19) depends on the instantaneous pressure and the temperature, and thus, the species

composition will depend on the atmospheric pressure at position z, $P_{STD}(z)$, and the surface temperature at the same position, $T_{SRF}(z)$.

The ATD Trajectory Tool (ATDTT) provides the ablated mass gradient $\Delta m/\Delta z$ during the re-entry which allows, together the atmospheric composition, to define the constraints in Eq. (16). The solution of GEM provides the vector of molar compositions $n = (n_1, n_2, n_3 \cdots n_N)$ or more precisely, the molar fractions $x = (x_1, x_2, x_3 \cdots x_N)$ with $\sum_i x_i = 1$.

These quantities allow the calculation of the mass fractions, $w = (w_1, w_2, w_3 \cdots w_N)$, for the N-species and then, the by-product amount emitted to the atmosphere at position z.

The thermochemical properties of the possible chemical compounds involved in the ablation process are expressed as NASA's up to 9th order temperature polynomials covering the temperature ranges from 200 K to 6000 K or even up to 20000 K depending on the polynomial order. The polynomial coefficients were taken from the Extended Third Millennium Ideal Gas and Condensed Phase Thermochemical Database, [38,41].

The equilibrium composition determined at P_{STD} and T_{SRF} must satisfy the constraint Eq. (16) where the vector b is the abundance vector or the atom conservation vector. Eq. (16) states that the total amount of atoms for a given element remains constant in the system. For closed systems, the vector b is just the atomic balance of the system, but for open systems, such as the by-product generation during the reentry, the strategy for the definition of the abundance vector, b, is different. Basically, the chemical reactions involved during the ablation of the materials at the atmospheric reentry are the oxidation of the materials involved. Since the atmosphere composition below 100 km is assumed constant, for the estimation of b it is enough to consider a great excess of air in the thermochemical calculation. If the air proportion is high enough, a further increase of this magnitude should return the same amount of the generated by-products since the ablating base material limits its production.

Considering this thermodynamic approach, four sequential steps must be considered to determine the chemical by-products emissions:

1. Compound identification in the whole database after the enumeration of the chemical elements initially present in the system
2. The atomic composition balance considering the initial chemicals and the air excess considered for the calculation
3. The Gibbs' Energy Minimisation itself
4. Data post-processing for the evaluation of by-product emission profiles along the reentry trajectory.

4.1. Compound identification

Considering the atom composition of the material subject to ablation process during the re-entry, the number of possible chemical by-products will be limited to all the possible recombination of these atoms. Together the atom composition of the ablated material, the oxygen and nitrogen of the atmosphere must be included as they react with these materials due to the high temperatures. Each of the by-products
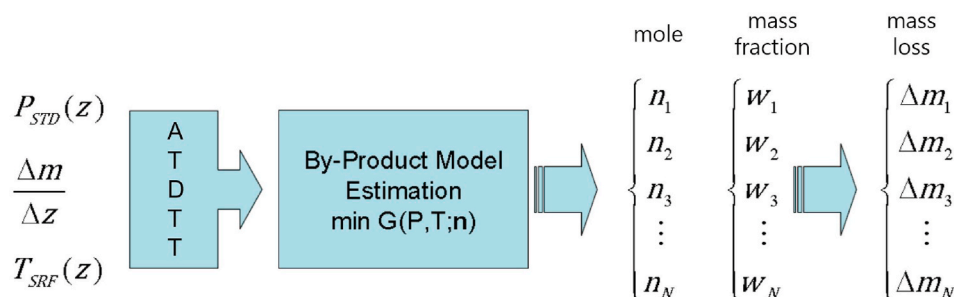

Fig. 2. The by-product emission simulation procedure.

has its own standard chemical potential and the final composition of the system will depend on the temperature, the pressure and the chemical potentials. The NASA and the Burcat's thermochemical databases ([38, 42,43], respectively) differ mainly on the number of chemical substances considered and the self-consistency of thermodynamic data. This self-consistency does not alter the final results of by-products proportions; the use of one database against the other is mainly justified by the higher number of possible substances defined in the database to be considered in the minimisation process. For instance, taking the AA7075-T6 alloy, which is a common structural material in spacecrafts and rocket bodies, the average composition by weight of this alloy is given in Table 1:

Assuming that all the elements of the AA7075-T6 will react with the air, the NASA and Burcat database provides the following possible by-products in Table 2:

The number of species in the extended Burcat database identifies additional possible by-products. These substances are however not in majority and they have a low thermochemical contribution to the overall chemical potential, thus, their molar fraction is low. The difference in the final composition calculated by both databases is hence small for the present conditions of pressure and temperature ranges of the atmosphere.

4.2. Atomic composition balance: stoichiometric requirements of air

As in a combustion database evaluation, the estimation of the air requirements ($O_2 + N_2$) passes by establishing the atomic basis for the thermochemical calculation, and this air excess needs to be considered for the estimation of the by-products. In the present works an air excess of 2.5 times the stoichiometric needs has been considered. Increasing this air excess, the calculation shows that the produced molar fraction of by-products remains unchanged confirming the oxygen excess conditions. As ATDTT performs the ablation calculation in weight units, the air quantity is evaluated as kg of air per kg of alloy. Assuming the above composition of the AA7075-T6 alloy, a 2.5 molar excess of air implies 8.46 kg-Air/kg-AA7075-T6 in the calculation.

4.3. Thermochemical calculation. Gibbs energy minimisation

The next step is the calculation of the composition of the by-products assuming that the surface temperatures of the ablated material is in equilibrium with all the components. It is necessary to solve Eqs. (15)–(19) using the atmospheric pressure and the surface temperatures changing with the altitude. Once the by-products are identified from the thermochemical databases, the oxygen and nitrogen quantities are determined by the stoichiometry of the ablated material. In the first iteration, all the chemical compounds are considered in the calculation and then, all the molar fractions of these substances are evaluated by minimisation. The contribution of each chemical substance to the Gibbs enthalpy will depend on the chemical potential of each substance. Here we are just interested in the major reactive components that could be released in the atmosphere. Hence we define a threshold value, ε, below which the substances are neglected (e.g. 1 ppm). Then, the air needs to be recalculated and the Gibbs Function minimisation is again iterated until convergence.

Table 3 shows the estimation of the by-products for the AA7075-T6 with an air excess using a molar fraction threshold of 10^{-6} and 10^{-20}. The molar fractions were estimated at atmospheric pressure $P_{STD} = 20.31$ Pa, and surface temperature $T_{SRF} = 900$ K, which is near the melting temperature of pure aluminium. The amount of the main

Table 1
AA7075-T6 alloy % composition.

Al	Zn	Mg	Cu	Cr
88.7%	6.1%	2.9%	2.0%	0.3%

Table 2
Identified species in the thermochemical databases compatible with the initial elements in the system. Some of the compounds identified in the Burcat database have different allotropic substances.

Phase	NASA	Burcat
Gas	Al, AlN, AlO, AlO$_2$, Al$_2$, Al$_2$O, Al$_2$O$_2$, Al$_2$O$_3$, Cr, CrN, CrO, CrO$_2$, CrO$_3$, Cu, CuO, Cu$_2$, Mg, MgN, MgO, Mg$_2$, N, NO, NO$_2$, NO$_3$, N$_2$, N$_2$O, N$_2$O$_3$, N$_2$O$_4$, N$_2$O$_5$, N$_3$, O, O$_2$, O$_3$, Zn	Al, AlN, AlO, AlO$_2$, Al$_2$, Al$_2$O, Al$_2$O$_2$, Al$_2$O$_3$, Cr, CrN, CrO, CrO$_2$, CrO$_3$, Cu, CuO, Cu$_2$, Mg, MgN, MgO, Mg$_2$, N, NO, NO$_2$, NOO, N$_2$O$_2$,NO$_3$, N$_2$, N$_2$O, N$_2$O$_3$, N$_2$O$_4$, N$_2$O$_5$, N$_3$, O, O$_2$, O$_3$, Zn, CrO, CuO, Cu$_2$, N$_4$, N$_4$, N$_4$, O*, O$_2$*, O$_3$c, O$_4$, ZnO
Condensed	Al(cr), Al(liq), AlN(cr), AlN(liq), Al$_2$O$_3$(a), Al$_2$O$_3$(liq), Cr(cr-a), Cr (cr-b), Cr(liq), CrN(cr), Cr$_2$N(cr), Cr$_2$O$_3$(I'), Cr$_2$O$_3$(I), Cr$_2$O$_3$(I), Cr$_2$O$_3$(I), Cr$_2$O$_3$(liq), Cu(cr), Cu (liq), CuO(cr), Cu$_2$O(cr), Cu$_2$O (liq), Mg(cr), Mg(liq), MgAl$_2$O$_4$(cr), MgAl$_2$O$_4$(liq), MgO (cr), MgO(liq), Mg$_3$N$_2$(cr), Zn (cr), Zn(liq)	Al(cr), Al(L), AlN(cr), AlN(L), Al$_2$O$_3$(a), Al$_2$O$_3$(liq), Cr(cr-a), Cr (cr-b), Cr(liq), CrN(cr), Cr$_2$N(cr), Cr$_2$O$_3$(I'), Cr$_2$O$_3$(I), Cr$_2$O$_3$(liq), Cu(cr), Cu(liq), CuO(cr), Cu$_2$O (cr), Cu$_2$O(liq), Mg(cr), Mg(L), MgAl$_2$O$_4$(cr), MgAl$_2$O$_4$(liq), MgO (cr), MgO(liq), Mg$_3$N$_2$(cr), Zn (cr), Zn(liq), ZnO
Ions	Al+, Al-, AlO+, AlO-, AlO$_2$-, Al$_2$O+, Al$_2$O$_2$+, Cr+, Cr-, CrO$_3$-, Cu+, Cu-, Mg+, N+, N-, NO+, NO$_2$-, NO$_3$-, N$_2$+, N$_2$-, N$_2$O+, O+, O-, O$_2$+, O$_2$-, Zn+	Al+, Al-, AlO+, AlO-, AlO$_2$-, Al$_2$O+, Al$_2$O$_2$+, Cr+, Cr-, CrO$_3$-, Cu+, Cu-, Mg+, N+, N-, NO+, NO$_2$-, NO$_3$-, N$_2$+, N$_2$-, N$_2$O+, O+, O-, O$_2$+, O$_2$-, Zn+ CrO$_3$-, NO-, NO$_2$+, NO$_2$+, NO$_2$-, NOO+, NOO-, NO$_3$+, NO$_3$-, N$_2$-, N$_2$O+, N$_2$O-, N$_2$O+, N$_2$O$_3$+, N$_2$O$_3$-, N$_3$+, N$_3$-, N$_4$-, O$_3$+, O$_3$-, O$_3$c+, O$_3$c-, O$_4$+, O$_4$-

metallic by-products, namely, Al$_2$O$_3$, Cr$_2$O$_3$, CuO, MgAl$_2$O$_4$, and ZnO are the same with independence of the threshold for the calculation of the molar fractions. Then, it is not necessary to reduce the molar fraction threshold to have the estimation of the majority by-products. The difference in the estimation of the main by-products differ by 0.29 ppm between $\varepsilon = 10^{-6}$ and 10^{-20}. Additionally, the mass of the minority by-products are in the range of grams while the majority ones are above the order of kilograms.

4.4. Data post-processing

To assess what could be the effect of these chemicals on atmospheric chemistry, for instance, the effect of the by-products on the depletion of the ozone layer. For this purpose it is necessary to have the emission rate of the by-products along the reentry trajectory to have the mass of the chemicals released as a function of the altitude. The ATDTT tool provides the ablated mass as a function of the altitude, i.e. $\frac{dm}{dz}$, together with the surface temperature. The GEM algorithm provides the molar fraction of each by-product as a function of the altitude. From these values, the total mass of each by-product released to the atmosphere is evaluated according to:

$$M_i(h) = \int_{z_{max}}^{z} w_i(P_{STD}, T_{SRF}; z) \left(\frac{dm}{dz}\right)_j dz \qquad (20)$$

where $M_i(h)$ is the accumulated mass of the i-th by-product released until the altitude z, with $0 \leq z \leq z_{max}$, $w_i(P,T; z)$ is the by-product mass fraction calculated from the thermochemical GEM code, P_{STD} is the instantaneous atmospheric pressure at the specific trajectory point, T_{SRF} the surface temperature, and $(dm/dz)_j$ is the ablated mass calculated from ATDTT. Eq. (20) provides the accumulated amount of the by-product generation summing up the instantaneous release of each chemical by-product along the re-entry trajectory.

Table 3
Molar fractions of by-products of AA7075 with air in excess evaluated at $T = 900$ K and $P = 20.31$ Pa; the first row shows the molar fraction threshold.

$\varepsilon = 10^{-6}$			$\varepsilon = 10^{-20}$		
Substance	phase	x_i	Substance	phase	x_i
NO	gas	$7.23\ 10^{-6}$	CrO_2	gas	$2.283\ 10^{-16}$
N_2	gas	0.812717	CrO_3	gas	$2.747\ 10^{-11}$
O_2	gas	0.125191	Cu	gas	$7.832\ 10^{-12}$
$Al_2O_3(a)$	Alpha	0.053428	CuO	gas	$4.282\ 10^{-14}$
$Cr_2O_3(I)$	Hexagonal	0.000101	Cu_2	gas	$1.829\ 10^{-20}$
CuO(cr)	Crystal	0.001103	NO	gas	$7.229\ 10^{-6}$
$MgAl_2O_4(cr)$	Crystal	0.004182	NO_2	gas	$9.643\ 10^{-9}$
ZnO	condensed	0.003269	NO_3	gas	$7.515\ 10^{-18}$
			N_2	gas	0.812723
			N_2O	gas	$9.987\ 10^{-12}$
			O	gas	$1.294\ 10^{-10}$
			O_2	gas	0.125192
			O_3	gas	$9.609\ 10^{-16}$
			Zn	gas	$2.074\ 10^{-11}$
			$Al_2O_3(a)$	Alpha	0.053429
			$Cr_2O_3(I)$	Hexagonal	0.000101
			CuO(cr)	Crystal	0.001103
			$MgAl_2O_4(cr)$	Crystal	0.004182
			CuO	gas	$4.282\ 10^{-14}$
			Cu_2	gas	$1.829\ 10^{-20}$
			O_2^*	gas	$2.851\ 10^{-7}$
			ZnO	condensed	0.003269
			ZnO	gas	$1.141\ 10^{-14}$

Table 4
Physical properties for test cases.

Case	Outer Radius (m)	Inner Radius (m)	Mass (kg)	Material
1	0.125	0.075	10.07	Graphite epoxy 1
2	0.125	0.029	12.685	Graphite epoxy 1
3	0.25	0.212	112.888	Titanium
4	0.25	0.212	40.28	Graphite epoxy 1
5	0.125	0.075	28.222	Titanium
6	0.125	0.076	28.222	Ti–6Al–4V
7	0.125	0.075	17.318	Aluminium
8	0.125	0.078	17.318	AA7075-T6

5. Results and discussion

5.1. Test cases

To evaluate the effect of thermochemical non-equilibrium (NEQ) flow on surface heat transfer and by-products generation, test cases are considered based on literature [44]. It is known that ORSAT by NASA and SCARAB by HTG (under ESA/ESOC contracts) are the representative object-oriented and spacecraft-oriented tools, respectively; they have been widely used and provide high accuracy simulation results [2,3,11, 15]. In literature, the comparison study between ORSAT and SCARAB was conducted and the results showed excellent agreement although they use different approaches for the calculation of trajectory, drag co-efficient, and thermal analysis [44]. The heat transfer and re-entry survival results were also compared and validated with that of the developed tool by the author's previous study [1,11]. In total, 120 different cases for simple-shaped objects (24 spheres, 48 cylinders, and 48 boxes) were considered with four different materials (aluminium, titanium, graphite epoxy 1 and 2).

In the references [11,44], the re-entry initial condition and test cases are determined and used in this study. For the initial condition, the altitude is 122 km, the relative flight path angle is −0.1°, the relative velocity is 7.41 km/s, the initial temperature is 300 K, the inclination angle is 28°, the latitude is 0°, and the longitude is 0°, respectively. For the test cases, the spheres made of graphite epoxy 1, titanium, Ti–6Al–4V, aluminium, and AA7075-T6 alloy were considered. Table 4

shows the detailed test cases. In this paper, we will mainly concentrate on metals and metallic alloys (cases 3 and 5–8).

The results of trajectory, Knudsen number, and net heat flux were compared and validated with those of ORSAT and SCARAB before analysing the post shock conditions, heat transfer, and by-products generation. The size of the body and the freestream conditions according to trajectory are significant factors that determine the post shock conditions. Therefore, the simulations have been performed to ensure the reliability of the ATDTT. The aforementioned tools assumed equilibrium (EQ) flow with fully catalytic wall condition in the heat transfer calculation. The present tool also used this assumption to be consistent for comparison purpose.

Fig. 3(a) and (b) represent altitude versus relative velocity and altitude versus time for case 1, respectively. It can be seen that the results of altitude versus relative velocity predicted by the present, ORSAT, and SCARAB are in good agreement. However, there is a discrepancy when the altitude is plotted against time. Particularly, the graph of SCARAB is noticeably shifted to the right in comparison to the others. The slightly different initial conditions and use of different Earth models are the main reason for the time differences. The present tool (ATDTT) described in this paper and ORSAT use a rotating spherical Earth, whereas SCARAB uses an oblate Earth. Due to decreasing radius of the oblate Earth in the direction of the poles, case 1 in SCARAB stays longer at a relatively high altitude with increasing latitude where there is less drag because of the presence of low air density [44]. However, as the altitude decreases, the graphs show the same shape without any remarkable influence on the magnitude of the results. The variation of Knudsen number for case 2 is presented in Fig. 4(a). The results show excellent agreement. The Knudsen number can be used to distinguish among three flow regimes (free molecular, transitional, and continuum flow). Fig. 4(b) shows the net heat flux over time for case 2. To compare the results of total heat flux (area of graph) in detail, time in abscissa is shifted for the time of maximum heating rate to be located on zero. It can be noted that the predicted net heat flux by three different tools are well matched by demonstrating that the difference in time has no significant effect on the re-entry survivability [11].
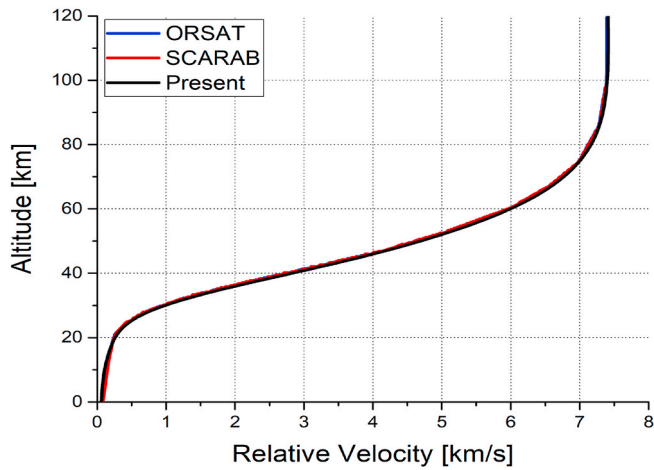
(a) Altitude variation with relative velocity
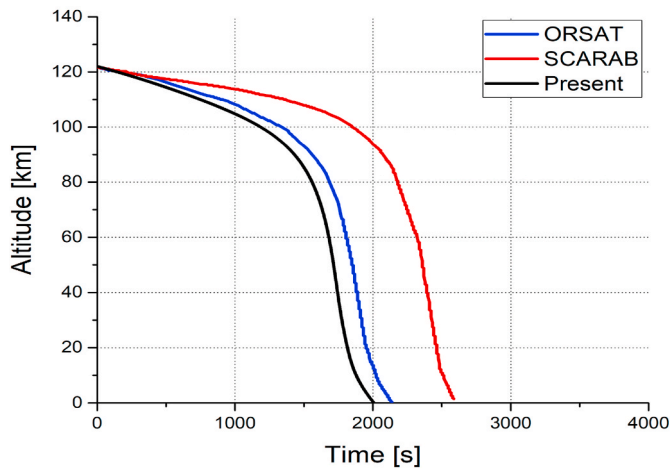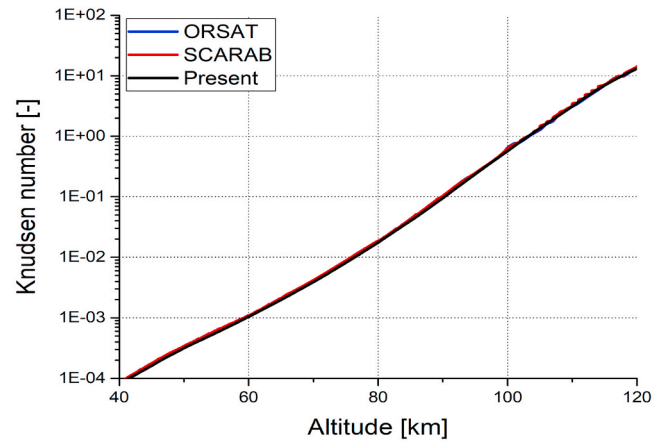

(b) Altitude variation with time

Fig. 3. Comparison with ORSAT and SCARAB for graphite epoxy 1 (case 1).

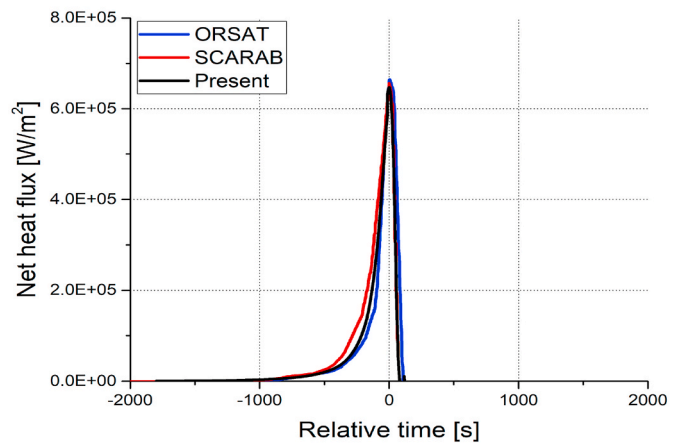(a) Knudsen number variation with altitude


(b) Net heat flux variation with time

Fig. 4. Comparison with ORSAT and SCARAB for graphite epoxy 1 (case 2).

5.2. Heat transfer analysis

5.2.1. Post shock relaxation data

In this section, thermochemical non-equilibrium effect on the post shock conditions was investigated. Figs. 5 and 6 show post shock relaxation profiles along the stagnation line for case 3. Two points of the case 3 re-entry trajectory have been simulated using the Park's three temperature model. The two points were considered to be within the continuum flow regime. The first point corresponds to an altitude of 45 km where the freestream density, temperature, pressure, and velocity are 0.002 kg/m^3, 264 K, 150 Pa, and 5.3 km/s, respectively. On the other hand, the second point corresponds to an altitude of 75 km where the freestream density, temperature, pressure, and velocity are 0.00004 kg/m^3, 208 K, 2.4 Pa, and 7.2 km/s, respectively.

Fig. 5 represents the temperature profiles behind a shock wave. Across the shock wave, most of the freestream kinetic energy is rapidly transformed into translational energy as they collide with the more dense shock layer gas. The caused collisions excite the molecular vibrational, rotational, and electronic modes, and then the translational energy begins to relax. In general, translational and rotational energy modes quickly equalise due to the energy transfer, while the vibrational and/or electronic excitations are considerably slower. From the large amount of energy, the molecules are also dissociated [28].

Looking at Fig. 5(a), the translational temperature immediately increases behind the shock wave with the assumption of frozen reactions. The temperature decreases further downstream as the oxygen and nitrogen molecules have sufficient time to dissociate. The vibrational temperature also increases and then decreases following the translational temperature. With the slowly increasing electron-electron temperature, the three temperatures reach a state of local equilibrium as they move to the surface of the object. Furthermore, the post shock equilibrium temperature has been calculated independently using the Chemical Equilibrium Compositions and Applications (CEA) program [45] and compared with the present results. The calculations made at an altitude of 45 km agree well with the equilibrium values computed by the CEA program. However, as can be seen in Fig. 5(b), the non-equilibrium temperatures do not reach the equilibrium state at an altitude of 75 km. Indeed, non-equilibrium effects are strong at such relatively high altitudes where the freestream density is low and the velocity is high, and the relaxation time is far too short to reach the equilibrium state.

Fig. 6 depicts the mole fraction profiles behind a shock wave at altitudes of 45 and 75 km, respectively. As mentioned in the previous section, the three temperature 11 species air model has been implemented in the calculation. The chemical equilibrium species calculated by the CEA program are also included for comparison. Looking at Fig. 6 (a), seven species (O, N, O$_2$, N$_2$, NO, O$^+$, NO$^+$) are presented. The other ionised species are excluded in the figure due to their small mole
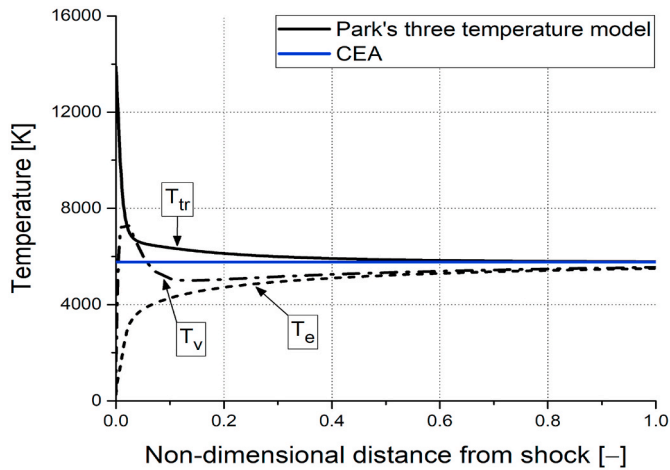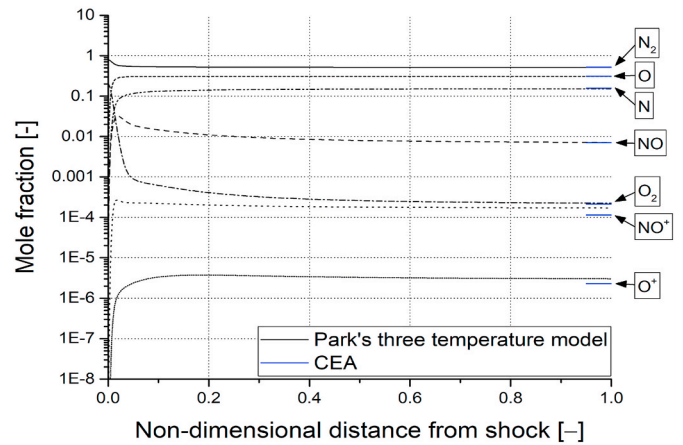
(a) At 45 km
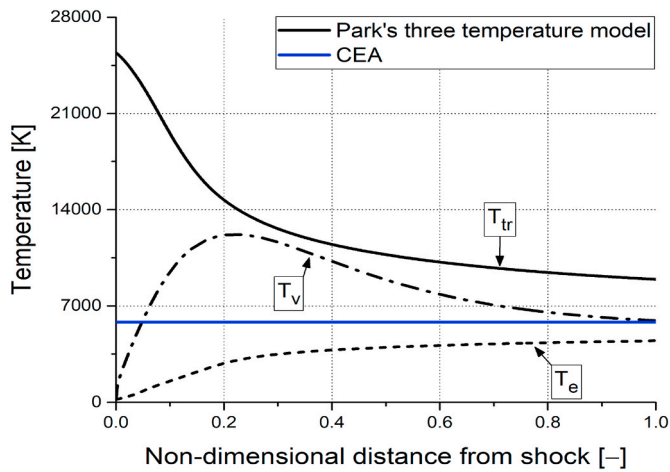
(b) At 75 km

Fig. 5. Comparison of post shock temperature profiles with CEA for titanium (case 3).

(a) At 45 km

(b) At 75 km

Fig. 6. Comparison of post shock mole fraction profiles with CEA for titanium (case 3).
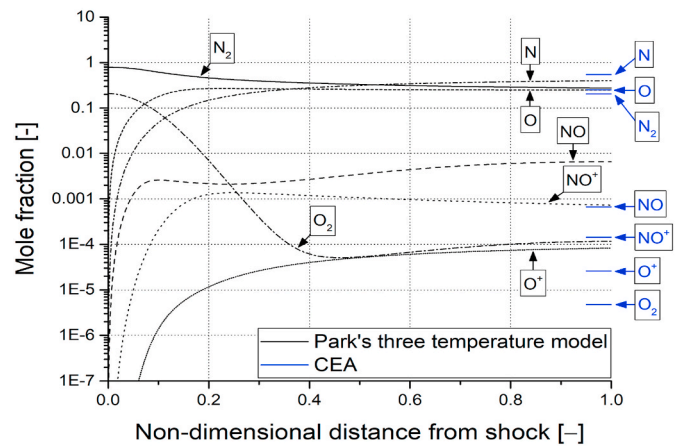
fractions (less than the order of 10^{-6}). It can be seen that the oxygen and nitrogen molecules are dissociated due to the large amount of thermal energy. In particular, the oxygen molecule is dissociated considerably and the dissociated atoms lead to high molar fractions of O, N, and NO. As can be seen in Fig. 5(a), all the species reach the equilibrium state further downstream. Overall, the present results show good agreement with that of the equilibrium flow at an altitude of 45 km. In Fig. 6(b), the species distribution at an altitude of 75 km is presented, where non-equilibrium effects are strong, and they are different from the values evaluated using an equilibrium flow assumption (CEA). Among them, the mole fractions of NO, NO^+, O^+, and O_2 are significantly different in the comparison.

5.2.2. Surface heat transfer data

The stagnation-point heat flux was investigated in this section. Figs. 7 and 8 represent the finalised calculated flow properties behind the shock wave and at the boundary layer edge for case 3 in Table 4. The values are also compared with that of the CEA program. The flow temperatures according to the re-entry trajectory are plotted in Fig. 7(a). There is a large discrepancy between non-equilibrium (NEQ) and equilibrium (EQ) flow at high altitude as already discussed in Fig. 5. However, at altitudes below about 50 km, the two results are quite well

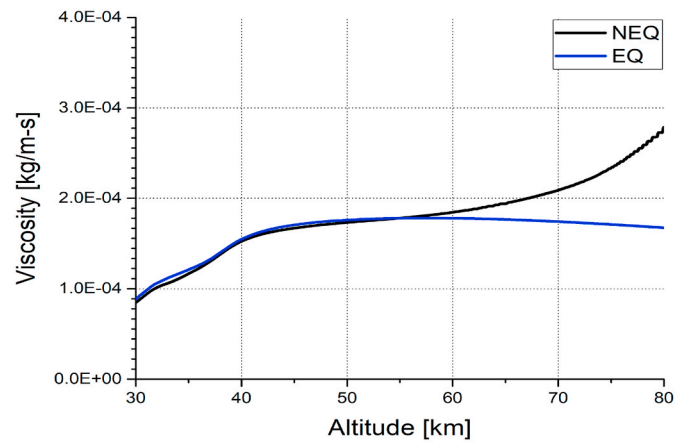matched each other, which means that non-equilibrium effects are strong at a relatively high altitude. Fig. 7(b) shows the density against altitude. It can be seen that the computed density is overall lower than that of the equilibrium flow although they agree quite well below at about 55 km. Fig. 8(a) shows the flow viscosity according to the altitude. The results are similar to the temperature profiles in Fig. 7(a) because the viscosity is computed based on the temperature [30]. The mass fraction of atomic nitrogen and oxygen versus altitude is presented in Fig. 8(b). Since the energy required to dissociate oxygen molecules is lower than that of the nitrogen, the high oxygen atom concentration is maintained until at an altitude of about 40 km. The oxygen mass fraction profiles in between non-equilibrium and equilibrium flow are in good agreement, while there is a large discrepancy in the nitrogen mass faction at altitudes above about 55 km. It should be noted that the equilibrium flow may overestimate the dissociated nitrogen atom concentration at high altitudes.

The stagnation-point heat transfer considering catalytic wall effect for cases 2 to 5 is presented in Fig. 9. In the simulations, the partial catalytic wall assumption was used. It is well known that a catalytic recombination coefficient varies along with the wall temperature and partial pressure of impinging atoms at the surface. Therefore, over the years, most of the coefficients have been obtained experimentally using different test facilities over a wide range of potential materials. According to literature, the catalytic efficiencies are usually in the range of
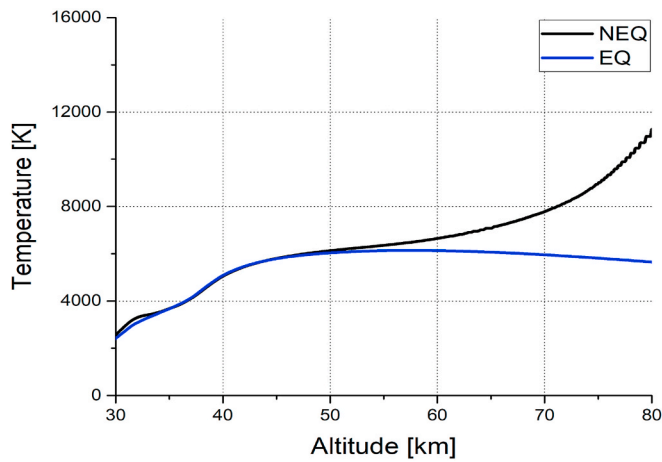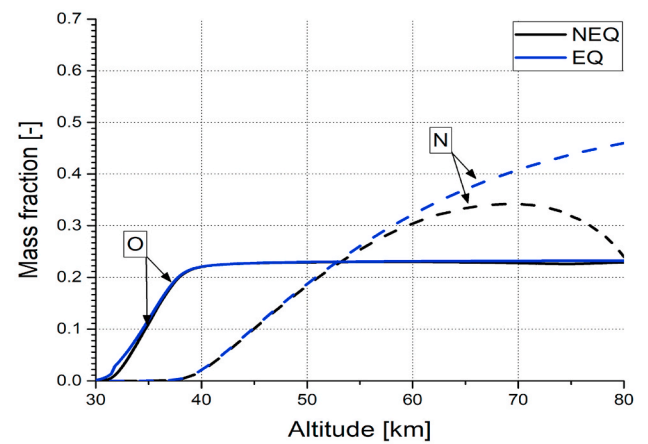
(a) Flow temperature variation
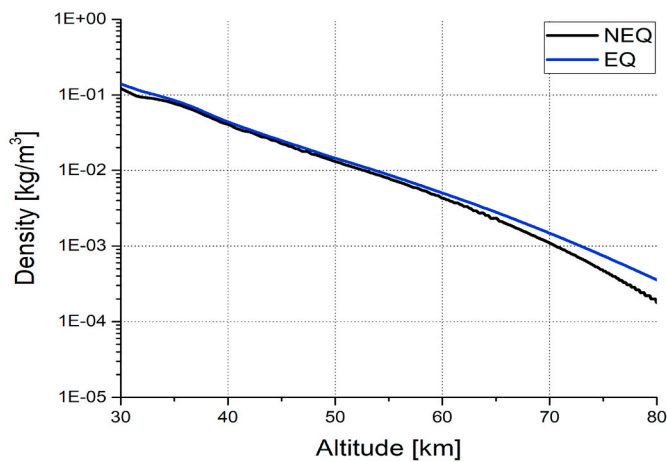
(b) Flow density variation

Fig. 7. Variation of flow temperature and density against altitude for titanium (case 3).

(a) Viscosity variation

(b) Mass fraction of nitrogen and oxygen atoms

Fig. 8. Variation of flow viscosity and atomic mass fraction against altitude for titanium (case 3).

0.001–0.1 for common materials such as Al, Fe, Ti, SiC, Al_2O_3, Fe_2O_3, TiO_2, and SiO_2, where the temperature is from room temperature to several thousands kelvins for a given partial pressure [11,34]. For this reason, in this study, the catalytic recombination coefficients for an oxygen and a nitrogen atom are assumed to be 0.01 regarding various flow regimes for the re-entry trajectory.

Fig. 9(a) shows the stagnation-point heat transfer for the titanium cases (cases 3 and 5) with a radius of 0.25 or 0.125 m. The heat flux calculated based on the equilibrium (EQ) flow is also given for comparison. As illustrated in the figure, from the re-entry point, the heat flux increases as the altitude decreases until its maximum heat flux is reached, and then it subsequently decreases. It can be seen that the present heat fluxes (designated by NEQ in the Figures) are higher than that of the equilibrium flow at high altitudes between 60 and 100 km, while they are lower at altitude ranges from 40 to 60 km where the maximum heat flux exists. The heat flux increases in proportion to the flow density and viscosity at the boundary layer edge according to the heat transfer theory. Although the density of the non-equilibrium flow is lower than that of the equilibrium flow, the viscosity is considerably higher in the region of high altitude as seen in Fig. 8(a). Therefore, the present results indicate higher heat flux at high altitudes. Meanwhile, at altitudes between 40 and 60 km, the present heat flux is quite lower compare to the equilibrium flow which has slightly larger values for

both the density and viscosity. For the altitudes between 60 and 100 km, the heat flux ratio of the equilibrium flow to the non-equilibrium flow for cases 3 and 5 in the largest discrepancy is 40.5% and 32.3%, respectively. Since the relaxation time to reach the equilibrium state is reduced as the size of the blunt body decreases, the non-equilibrium effect on case 5 is more dominant than that of case 3. However, for the altitudes between 40 and 60 km, the heat flux ratio of the equilibrium flow to the non-equilibrium flow for cases 3 and 5 is 107.8% and 108.5%, respectively.

A similar observation is made for the stagnation-point heat transfer for the Graphite epoxy 1 cases (cases 2 and 4) in Fig. 9(b). For the altitudes 40–60 km and 60–100 km, the heat flux ratio of the equilibrium flow to the non-equilibrium flow for cases 2 and 4 in the largest discrepancy is 103.7% and 103.2%, and 37.4% and 49.3%, respectively. Although the discrepancy in heat flux at altitude ranges from 40 to 60 km is quite negligible, the large discrepancy is still observed at high altitudes. In Fig. 9, for the worst case re-entry scenario, the test cases made of titanium and graphite epoxy 1 having a relatively high heat of fusion were considered to analyse heat transfer by avoiding ablation. Fig. 10 shows the comparison of integrated stagnation-point heat transfer for cases 2 to 5. The integrated heat flux versus altitude and integrated heat flux versus time are presented in Fig. 10(a) and (b), respectively. The integrated heat flux has a significant effect on the amount of materials ablation and consequently it is directly related to the re-entry survivability. As can be seen in Fig. 9, at altitudes between
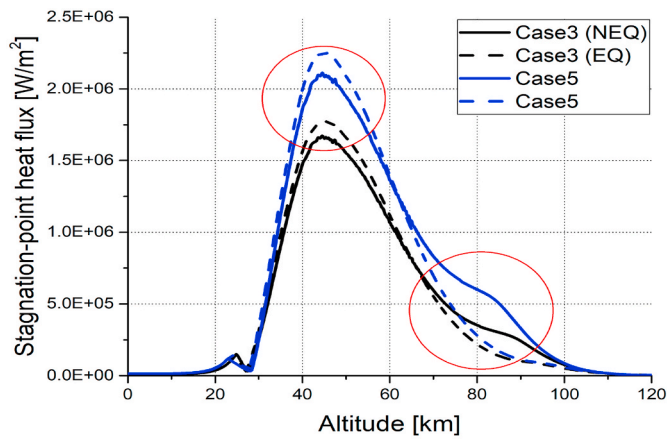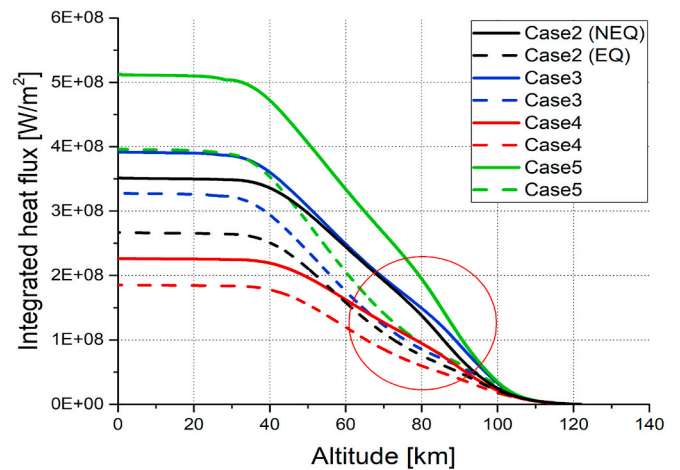
(a) Titanium
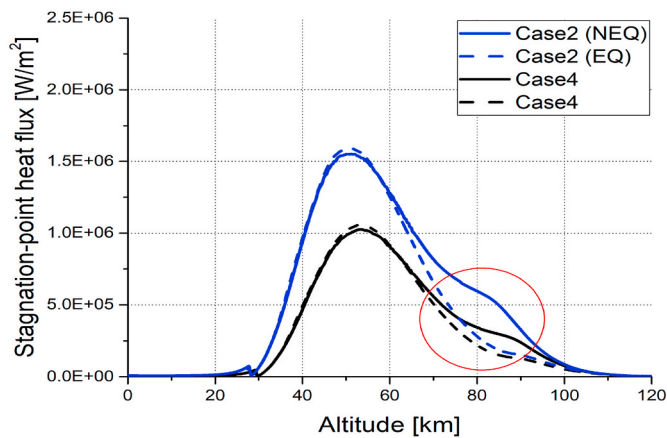
(b) Graphite epoxy 1

Fig. 9. Stagnation-point heat flux against altitude for titanium and graphite epoxy 1 (cases 2 to 5).

(a) Integrated heat flux variation with altitude


(b) Integrated heat flux variation with time

Fig. 10. Comparison of integrated stagnation-point heat flux for cases 2 to 5.

60 and 100 km, the difference in the integrated heat flux between non-equilibrium and equilibrium flow increases rapidly for each case. The final integrated heat flux ratio of the equilibrium flow to the non-equilibrium flow for cases 2 to 5 is 75.9%, 83.7%, 81.9%, and 77.3%, respectively.

5.3. By-products results and analyses

The coupling of the ATDTT tool and the GEM tool allows a detailed by-product analysis along the trajectory paths. The simulations in the ATDTT tool are performed using equilibrium air chemistry post shock assumptions (EQ) and non-equilibrium ones (NEQ). In this paper, generic metals and metal alloys that are significant for satellite structures and components are considered in detail. In Fig. 11, titanium and the alloy Ti–6Al–4V are considered. The composition of this alloy varies within the ranges as follows (see Table 5):

The alloy AA7075-T6 composition is given in Table 1 previously. The average composition of Ti–6Al–4V alloy is mainly Ti 90%, V 4% and Al 6% in weight. Then, the stoichiometric oxygen needs for the complete ablation of this alloy is 2.58 kg air/kg Ti–6Al–4V. Due to the high melting temperature of these alloys, the total ablated mass is much lower than the AA7075-T6 type alloys. It is clear from Figs. 11 and 12, that the non-equilibrium post shock chemistry (designated by NEQ in the figures) has a significant impact on the level of the by-product estimations. Only the main substances obtained are depicted, and the roles

of the metallic oxides are significant as well as NO production.

In Fig. 11(a) and (b), the by-product estimations for the titanium cases are shown. The ablated mass and surface temperature are simulated by the ATDTT code. As pure titanium and the titanium alloys are difficult to demise, the differences for the metallic oxides are small as the ablative masses are similar. However, their production covers a wide altitude span also at lower altitudes, which entails that particles of titanium dioxide for instance are still present and could even drift into the atmospheric ozone layer where they would have a significant impact. Indeed we can clearly see that the crystalline states of TiO_2 are in greater quantities than the gas phase ones. This oxide could have some relevance on the ozone atmospheric chemistry due to the photocatalytic activity of TiO_2 against ozone decomposition. However, we can notice that there is a relatively small quantity formed which limits such an effect.

In Fig. 12(a) and (b), the emission profiles for the aluminium cases are studied. The main influence of the non-equilibrium air chemistry modelling is the altitude shift. The debris is consumed starting from the beginning of the re-entry just after 80 km in the non-equilibrium modelling case (NEQ), whereas the ablation only starts around 60 km for the equilibrium chemistry case (EQ). The importance here is the production of oxides at higher altitudes, the particles of these by-products will remain for more time within the atmosphere in the NEQ
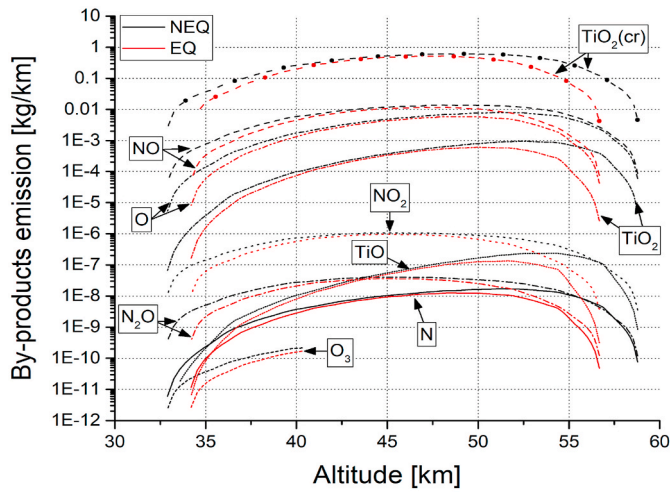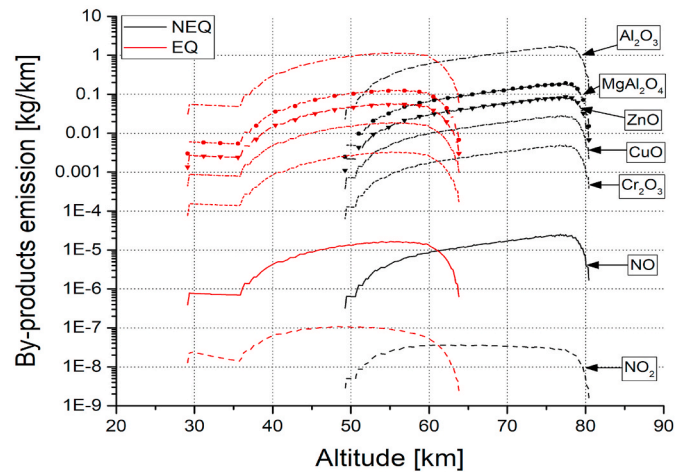
(a) Titanium (case 5)
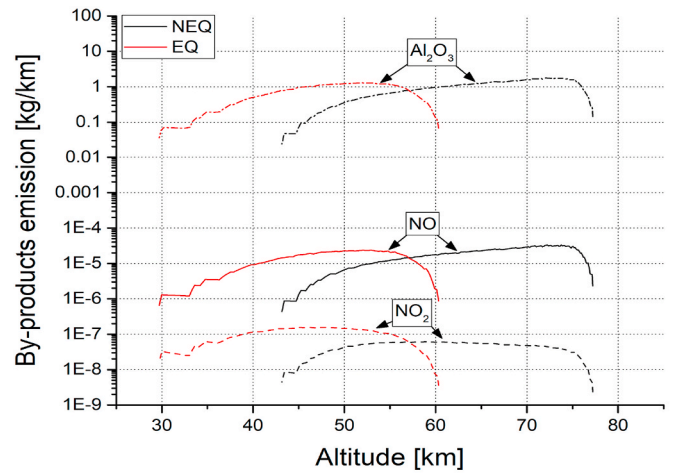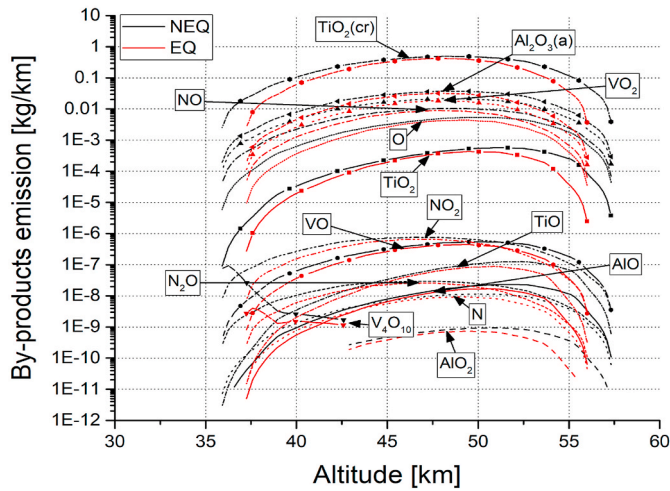
(b) Ti-6Al-4V (case 6)

Fig. 11. By-products generation against altitude for titanium and Ti–6Al–4V (results represent instantaneous emission of by-products per unit altitude).

Table 5
Ti–6Al–4V % composition.

Ti	Al	V	Fe	O	C
87.7–91%	5.5–6.75%	3.5–4.5%	0–0.3%	0.2%	0–0.08%

case than in the EQ case, which will have a long-term impact on atmospheric chemistry.

There is an evident correlation between the total ablated mass calculated with the ATDTT code and the emitted oxide mass where the total amount depends on the element proportion in the initial alloy. Then, the aluminium and the aluminates, i.e. Al_2O_3 and $MgAl_2O_4$ respectively, are the most abundant by-products produced during the re-entry and the ablation of the satellite debris. The Zn and Cu components of the alloy are basically vaporised in gas phase except a small quantity of CuO formed at high altitude, where the temperatures are relatively lower and the low oxygen partial pressure here leads to the formation of this more stable oxide.

Both Figs. 11 and 12 show also how the by-products are the results of air decomposition at high temperatures. There is a correlation between

(a) Aluminium (case 7)

(b) AA7075 T6 (case 8)

Fig. 12. By-products generation against altitude for aluminium and AA7075-T6 (results represent instantaneous emission of by-products per unit altitude).

the temperature and the molar fractions of the NO, O and excited oxygen molecule, O_2^*. The higher the temperature, the higher the NO, and O concentrations. The atomic oxygen formation is also affected by the oxygen partial pressure in the atmosphere showing a higher concentration at higher altitudes because its low recombination rate at these low pressures. The high surface temperature reached for these alloys could increase the nitrogen oxides and atomic oxygen by the air decomposition. Assuming the equilibrium condition just near the ablated surface, it is possible to evaluate the molar fractions profiles for the NO, O and the excited oxygen molecule, O_2^*, along the re-entry trajectory. However, the realistic quantity of these compounds released in the atmosphere is also associated to the form and distance of the shockwave in front of the debris object during its re-entry (which can be a complex process as the object is tumbling, changes form and orientates itself differently - change of entry angle with time). Here we have taken into account the post-shock chemistry, which in itself is an important improvement.

The thermochemical calculations show that the most stable by-products attainable during a re-entry event from the ablation of the metal alloys are the metal oxides at their higher oxidation state. Here we have determined the composition at the pressure and temperature conditions during the re-entry. Combining this information with the

ablation rate along the re-entry trajectory for the different materials, it is possible to estimate the by-product emissions. These quantities suppose the maximum allowable quantity of the emitted chemicals in the atmosphere, rendering the upper limit for the possible effect on the atmospheric chemistry. The boundary layer between the re-entering object surface and the shock wave is a region with an extremely high chemical activity. On one side, the gas chemistry is governed by the dissociation-recombination reactions between the N_2 and O_2 together with minor atoms and molecules present behind the shock wave. The high temperature here dissociates both molecules generating atomic oxygen and nitrogen. The recombination of these atoms lead to the formation of nitrogen oxides as the thermochemical analysis predicts. On the other hand, the chemistry at the surface of the re-entering object is governed by the presence of these highly reactive gas species such as the atomic oxygen and the ablation mechanisms that could potentially proceed through and enhance oxidation mechanisms instead a simple melting or sublimation process. The high temperatures and high atomic oxygen concentrations near the surface will lead to a fast growth of the oxide layer in the metallic surface, particularly in highly reactive metals like the aluminium (plus alloy) one which weakly remains in metallic form under such as oxidant environment. Our results confirm this hypothesis. The ablation leads to the formation of alumina or aluminates, i. e. Al_2O_3 and $MgAl_2O_4$, respectively. The temperature is not high enough to oxidise the Cu and Zn, these metals sublimate from the AA7075-T6 alloy. Even if these metallic oxides are formed, the CuO can react with the metallic Al to be reduced to Cu and the low boiling point of the Zn lead to the sublimation of this metal.

The same arguments are valid for the titanium cases despite the lower quantities of formation of the metal oxides due to a higher melting temperature.

There are also some experimental evidences supporting the oxidative ablation mechanisms. Recent projects within Plasma Wind Tunnel facilities at the Institute of Space Systems (IRS) at the University of Stuttgart have investigated the ablation of metals and alloys under the typical reentering condition for the spacecraft, in particular AA7075-T6 aluminium, AISI 316L steel, Ti–6Al–4V titanium alloy, silicon carbide (SiC) and one type of carbon fibre reinforced plastic (CFRP) [46]. The observations showed systematically the surface oxidation with partial ejection of oxide layers and growth of new ones, surface oxidation and deposit of spilled material on top of the surface for stainless steel and surface oxidation together possible vaporisation of low melting elements for aluminium alloys. This last observation is consistent with in our evaluations. These experiments also agree with the observations done by Préveraud et al. [47] at the MESOX facility in the PROMES-CNRS laboratory.

5.4. Ground risk assessment due to break-up

The re-entry trajectory of space debris due to break-up was analysed in this section. Particularly, the effect of non-equilibrium flow on the break-up altitude was noted, and the ground footprint and downrange according to the altitude were investigated. Generated by-products by material ablation were also calculated in the analysis. For the break-up mechanism, it was assumed that thermal break-up (melting) is only considered using the parent and child relationship, which is a concept that a single main object such as a spacecraft contains all the other components [6]. According to literature, the break-up usually occurs at an altitude in the range between 75 and 85 km, and the break-up altitude of 78 km is mainly used for the re-entry simulation [2,6]. Hence, the initial test case was modelled assuming it breaks at 78 km based on the equilibrium flow.

The generic satellite was considered as the test case (parent model) with the size of 1.2 m, and it was modelled as a box with the randomly tumbling motion. General aluminium was used as the material to mainly focus on the non-equilibrium flow effect and its mass was 62 kg. Cases 3 and 4 in Table 4 were used as inner components (child model); titanium

and graphite epoxy 1 which have a high heat of fusion were used as the material to thoroughly examine the ground footprint and downrange by avoiding ablation. Additionally, cases 3 and 4 (fully solid spheres) with the inner radius of 0 were also considered for the inner components. Therefore, the mass of cases 3 and 4 (hollow) and cases 3 and 4 (solid) were 112.89 kg and 40.28 kg, and 287.98 kg and 102.766 kg, respectively. For the re-entry initial conditions, values presented in literature [26] were used. The initial test case has been analysed using two different flow approaches: non-equilibrium (NEQ) and equilibrium (EQ) flow.

Fig. 13 represents the by-products generation according to altitude. Since the inner cases do not ablate after the satellite break-up, the estimated chemical compositions, which are induced from the satellite, are mainly AlO_2, NO, NO_2, and O. It is noted that the by-products are generated until the satellite is completely demised. Although the amount of the chemical compositions for the equilibrium and non-equilibrium flows are similar due to the complete demise, there is a large discrepancy between the two different flows for the break-up and by-products emission altitude.

Fig. 14 shows the re-entry trajectory profiles in terms of altitude and downrange. Altitude versus downrange is presented in Fig. 14(a). The results show that the test case break-up occurs at about 78 km for the equilibrium flow, while it occurs at about 91 km for the non-equilibrium flow. As already discussed in Fig. 9, at high altitudes, the higher stagnation-point heat transfer for the non-equilibrium flow was observed than that of the equilibrium flow. Therefore, it can be seen that the higher heat flux exists at the surface in the region of high altitude, the higher thermal break-up altitude is determined and consequently the equilibrium flow can underestimate the break-up altitude compared to the non-equilibrium flow. Furthermore, a large discrepancy in the downrange of each inner case is also observed with respect to the break-up altitude. After the break-up, the calculated ballistic coefficients (m/ c_d·A) of cases 3 (hollow), 4 (hollow), 3 (solid), and 4 (solid) corresponding to the break-up altitude of 91 km were 410.77 kg/m^2, 146.73 kg/m^2, 1047.89 kg/m^2, and 373.9 kg/m^2, respectively; the ballistic coefficients corresponding to the break-up altitude of 78 km were 527.84 kg/m^2, 188.34 kg/m^2, 1346.52 kg/m^2, and 480.46 kg/m^2, respectively.

Fig. 14(b) shows altitude versus time for each case. It can be seen that the difference in downrange for the non-equilibrium flow modelling is larger than that of the equilibrium flow one since for all the cases, except case 4 (hollow), with a break-up altitude of 91 km maintain a relatively higher altitude than those with the break-up altitude of 78 km. The results in Fig. 14 indicate that as the break-up altitude increases, the
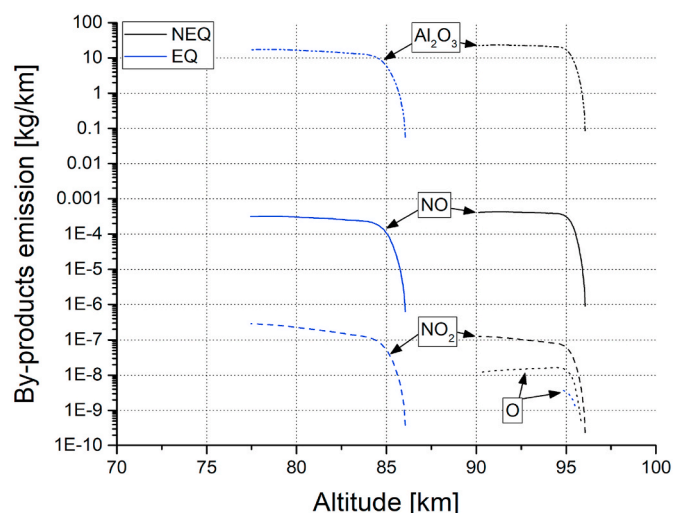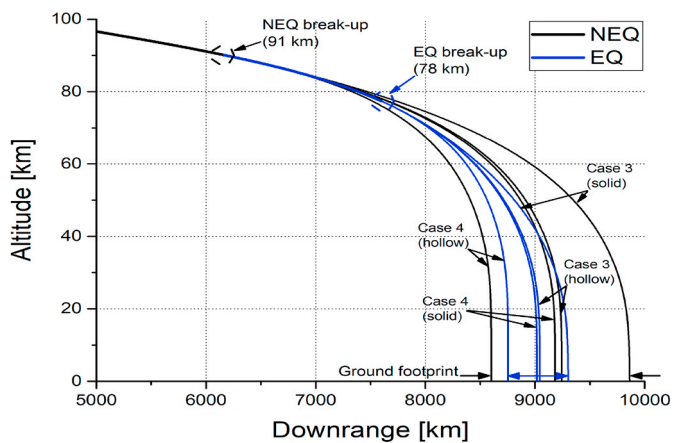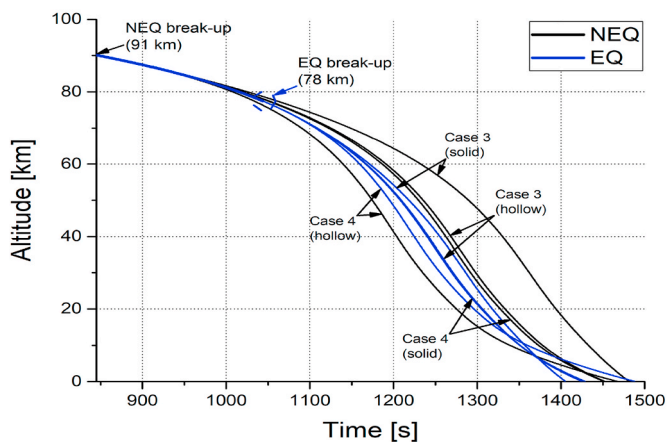

Fig. 13. By-products generation for a generic aluminium satellite.

(a) Altitude vs. downrange

(b) Altitude vs. time

Fig. 14. Re-entry trajectory estimation for the generic aluminium satellite break-up.

difference in the ground footprint as well as the downrange of re-entry objects increases, implying the importance of the implementation of the non-equilibrium flow approach to the re-entry analysis, especially for the break-up at high altitudes.

6. Conclusions

Re-entry survivability and ground risk estimations of space debris have been conducted by considering by-products generation. Particular attention is focused on the use of the space components materials such as metals and metal alloys. Non-equilibrium air chemistry effects are taken into account using the Poshax3, which is a post shock relaxation solver developed at the University of Queensland. It was combined with the authors' developed re-entry analysis tool. The three-temperature, 11-species air model and the energy exchange models by Park and Gnoffo were considered in the present work. The generated chemical by-products according to the ablation at the surface during re-entry were also estimated using a Gibbs energy minimisation procedure.

To ensure the reliability of this coupled tool (named 'ATDTT'), the results of trajectory and heat flux were validated with those of existing tools assuming the equilibrium flow with fully catalytic wall condition. Spheres made of various materials were used as the test models. Then, based on the non-equilibrium flow with partially catalytic wall condition, the post shock conditions, heat flux, and by-products generation according to the re-entry trajectory within the continuum flow regime

were investigated, and the results were compared with those of the equilibrium flow estimated using the CEA program. It was found that there is a large discrepancy in flow properties and produced chemical compositions at high altitudes, with a significant difference in heat flux calculation.

Furthermore, the ground risk assessment due to break-up was conducted to further examine the effect of non-equilibrium flow at high altitudes. In the simulation, the generic satellite including four different inner components was tested, and thermal break-up assumption was used. The results have shown that as the break-up altitude increases, the difference in the ground footprint as well as the altitude of generated by-products from re-entry objects increases. It is to be noted that the higher heat flux exists at the surface in the region of high altitude, the higher ablation rate is determined and consequently the equilibrium flow can underestimate the by-products emission and break-up altitude, implying the importance of the implementation of the non-equilibrium flow and by-products generation approaches to the re-entry analysis. In conclusion, it is clear that non-equilibrium effects impact the ablation rate and the by-products emissions at high altitude.

Declaration of competing interest

The authors declare that they have no known competing financial interests or personal relationships that could have appeared to influence the work reported in this paper.

References

[1] S.-H. Park, H.-D. Kim, G. Park, Orbit, orbital lifetime, and reentry survivability estimation for orbiting objects, Adv. Space Res. 62 (11) (2018) 3012–3032, https://doi.org/10.1016/j.asr.2018.08.016.

[2] T. Lips, B. Fritsche, A comparison of commonly used re-entry analysis tools, Acta Astronaut. 57 (2–8) (2005) 312–323, https://doi.org/10.1016/j.actaastro.2005.03.010.

[3] T. Lips, B. Fritsche, G. Koppenwallner, Spacecraft destruction during re-entry - latest results and development of the scarab software system, Adv. Space Res. 34 (5) (2004) 1055–1060, https://doi.org/10.1016/j.asr.2003.01.012.

[4] B. Fritsche, T. Lips, G. Koppenwallner, Analytical and numerical reentry analysis of simple-shaped objects, Acta Astronaut. 60 (8–9) (2007) 737–751, https://doi.org/10.1016/j.actaastro.2006.07.017.

[5] C. Ostrom, C. Sanchez, Orsat Modelling and Assessment (03 2018). doi: 10.13140/RG.2.2.26944.64001.

[6] I.P. Fuentes, D. Bonetti, F. Letterio, G.V. de Miguel, G.B. Arnao, P. Palomo, C. Parigini, S. Lemmens, T. Lips, R. Kanzler, Upgrade of esa's debris risk assessment and mitigation analysis (drama) tool: spacecraft entry survival analysis module, Acta Astronaut. 158 (2019) 148–160, https://doi.org/10.1016/j.actaastro.2017.12.001.

[7] J. Annaloro, S. Galera, C. Thiebaut, M. Spel, P. Van Hauwaert, G. Grossir, S. Paris, O. Chazot, P. Omaly, Aerothermodynamics modelling of complex shapes in the debrisk atmospheric reentry tool: methodology and validation, Acta Astronaut. 171 (2020) 388–402, https://doi.org/10.1016/j.actaastro.2020.03.006. http://www.sciencedirect.com/science/article/pii/S009457652030134X.

[8] M. Ivanov, Statistical Simulation of Reentry Capsule Aerodynamics in Hypersonic Near-Continuum Flows, NATO AVT STO reports, EN-AVT-194-18, 2011.

[9] P.M. Mehta, M. Kubicek, E. Minisci, M. Vasile, Sensitivity analysis and probabilistic re-entry modeling for debris using high dimensional model representation based uncertainty treatment, Adv. Space Res. 59 (1) (2017) 193–211, https://doi.org/10.1016/j.asr.2016.08.032.

[10] S.F. Rafano Carna, R. Bevilacqua, High fidelity model for the atmospheric re-entry of cubesats equipped with the drag de-orbit device, Acta Astronaut. 156 (2019) 134–156, https://doi.org/10.1016/j.actaastro.2018.05.049.

[11] S.-H. Park, G. Park, Reentry trajectory and survivability estimation of small space debris with catalytic recombination, Adv. Space Res. 60 (5) (2017) 893–906, https://doi.org/10.1016/j.asr.2017.05.004.

[12] R. Herman, Hypersonic non-equilibrium flow and its thermodynamic relations, in: Proceedings of the 4th Space Symposium, 1965, pp. 893–906.

[13] G. Park, S.L. Gai, A.J. Neely, Laminar near wake of a circular cylinder at hypersonic speeds, AIAA J. 48 (1) (2010) 236–248, 10. 2514/1.44167.

[14] J.D. Anderson, Hypersonic and High Temperature Gas Dynamics, second ed., AIAA Education Series, 2006.

[15] W.C. Rochelle, R.E. Kinsey, E.A. Reid, R.C. Reynolds, N.L. Johnson, Spacecraft Orbital Debris Reentry Aerothermal Analysis, Proceeding of the 8ᵗʰ Annual Thermal and Fluids Analysis Workshop Spacecraft Analysis and Design, 1997.

[16] J. Navarro Laboulais, P. Leyland, E. Goos, S. Bianchi, S. Mischler, L. Grassi, By-product Emission Analyses for Atmospheric Impact of Re-Entering Space Debris (submitted for publication), Aerospace Science and Technology, 2020.

[17] L.O. Cropp, Analytical Methods Used in Predicting the Re-entry Ablation of Spherical and Cylindrical Bodies, Sandia Corporation SC-RR, 1965, pp. 65–187.

[18] R.D. Klett, Drag Coefficients and Heating Ratios for Right Circular Cylinders in Free-Molecular and Continuum Flow from Mach 10 to 30, Sandia Corporation SC-RR-64-2141, 1964.

[19] G. Koppenwallner, B. Fritsche, T. Lips, H. Klinkrad, Scarab -a multi-disciplinary code for destruction analysis of space-craft during re-entry 563, European Space Agency, (Special Publication) ESA SP, 2005, p. 281.

[20] P. Vashchenkov, M. Ivanov, A. Krylov, G. Markelov, Numerical simulations of high-altitude aerothermodynamics of a promising spacecraft model, AIP Conf. Proc. 1333 (2011) 1337–1342, https://doi.org/10.1063/1.3562829.

[21] M. Trisolini, H.G. Lewis, C. Colombo, Demisability and survivability sensitivity to design-for-demise techniques, Acta Astronaut. 145 (2018) 357–384, https://doi.org/10.1016/j.actaastro.2018.01.050.

[22] C.-O. Min, D.-W. Lee, Reentry analysis and risk assessment for end-of-life disposal of a multi-layer leo satellite, Int. J. Aeronaut. Space Sci. 19 (2018) 496–508, https://doi.org/10.1007/s42405-018-0036-0.

[23] H.S. Sim, K.H. Kim, Reentry survival analysis of tumbling metallic hollow cylinder, Adv. Space Res. 48 (5) (2011) 914–922, https://doi.org/10.1016/j.asr.2011.04.036.

[24] R.L. Kelley, W.C. Rochelle, Atmospheric Reentry of a Hydrazine Tank, NASA White paper, Houston, TX, 2012, pp. 1–11.

[25] J.-C. Liou, J.N. Opiela, A.B. Vavrin, B. Draegar, P.D. Anz-Meador, C.L. Ostrom, C. Sanchez, Debris Assessment Software User's Guide: Version 3.0, NASA, 2019. https://orbitaldebris.jsc.nasa.gov/mitigation/debris-assessment-software.html.

[26] S.-H. Park, G. Park, Separation process of multi-spheres in hypersonic flow, Adv. Space Res. 65 (1) (2019) 392–406, https://doi.org/10.1016/j.asr.2019.10.009.

[27] R.J. Gollan, The Computational Modelling of High-Temperature Gas Effects with Application to Hypersonic Flows, Ph.D. Thesis, University of Queensland, 2008.

[28] D.F. Potter, Modelling of Radiating Shock Layers for Atmospheric Entry at Earth and Mars, Ph.D. Thesis, University of Queensland, 2010.

[29] C. Park, Review of chemical-kinetic problems of future nasa missions, I: Earth entries, J. Thermophys. Heat Tran. 7 (3) (1993) 385–398, https://doi.org/10.2514/3.431.

[30] P.A. Gnoffo, R.N. Gupta, J.L. Shinn, Conservation Equations and Physical Models for Hypersonic Air Flows in Thermal and Chemical Nonequilibrium, Technical Report, NASA-TP-2867, 1989.

[31] R.N. Gupta, J.M. Yos, R.A. Thompson, K.-P. Lee, A Review of Reaction Rates and Thermodynamic and Transport Properties for an 11-species Air Model for Chemical and Thermal Nonequilibrium Calculations to 30,000 K, Technical Report, NASA-RP-1232, 1990.

[32] H. Serbin, Supersonic flow around blunt bodies, J. Aeronaut. Sci. 25 (1) (1958) 58–59, https://doi.org/10.2514/8.7487.

[33] S.-H. Park, G. Park, Separation process of spheres in hypersonic flows, in: 2018 AIAA Atmospheric Flight Mechanics Conference, Kissimmee, Florida, AIAA-2018-0288, 2018, https://doi.org/10.2514/6.2018-0288.

[34] R. Goulard, On catalytic recombination rates in hypersonic stagnation heat transfer, J. Jet Propuls. 28 (11) (1958) 737–745, https://doi.org/10.2514/8.7444.

[35] W. Smith, W. Qi, Molecular simulation of chemical reaction equilibrium by computationally efficient free energy minimization, Acs Central Sci. 4 (9) (2018) 1185–1193, https://doi.org/10.1021/acscentsci.8b00361.

[36] W.R. Smith, R.W. Missen, Chemical Reaction Equilibrium Analysis: Theory and Algorithms, John Wiley and Sons, 1982.

[37] W.R. Smith, R.W. Missen, Strategies for solving the chemical equilibrium problem and an efficient microcomputer-based algorithm, Can. J. Chem. Eng. 66 (4) (1988) 591–598, https://doi.org/10.1002/cjce.5450660409.

[38] A. Burcat, Thermochemical species in polynomial form. https://burcat.technion.ac.il/, 2019.

[39] B. Kelly, W. Smith, Molecular simulation of chemical reaction equilibria by kinetic Monte Carlo, Mol. Phys. (2018) 1–8, https://doi.org/10.1080/00268976.2018.1552027.

[40] C.H. Turner, J.K. Brennan, M. Lisal, W.R. Smith, J. Karl Johnson, K.E. Gubbins, Simulation of chemical reaction equilibria by the reaction ensemble Monte Carlo method: a review, Mol. Simulat. 34 (2) (2008) 119–146, https://doi.org/10.1080/08927020801986564. http://www.tandfonline.com/doi/abs/10.1080/08927020801986564.

[41] A. Burcat, B. Ruscic, Third Millenium Ideal Gas and Condensed Phase Thermochemical Database for Combustion (with update from active thermochemical tables), Tech. Rep., Argonne National Laboratory (ANL), Argonne, IL, jul 2005, https://doi.org/10.2172/925269 http://www.osti.gov/servlets/purl/925269-199FKl/.

[42] NASA Glenn Research Center, Chemical equilibrium with Applications (CEA-NASA). https://www.grc.nasa.gov/WWW/CEAWeb/, 2019.

[43] B.J. McBride, S. Gordon, M.A. Reno, Coefficients for calculating thermodynamic and transport properties of individual species, NASA Tech. Memo. 4513 (1993).

[44] T. Lips, V. Wartemann, G. Koppenwallner, H. Klinkrad, D. Alwes, R.N.S.J. Dobarco-Otero, R.M. DeLaune, W.C. Rochelle, N.L. Johnson, Comparison of Orsat and Scarab Reentry Survival Results, 4ᵗʰ European Conference on Space Debris, ESA/ESOC, Darmstadt, Germany, 2005.

[45] S. Gordon, B.J. McBride, Computer Program for Calculation of Complex Chemical Equilibrium Composition and Applications. Part 1: Analysis, Technical Report, vol. 1311, NASA-RP, 1994.

[46] A.S. Pagan, B. Massuti-Ballester, G.H. Herdrich, Experimental thermal response and demisability investigations on five aerospace structure materials under simulated destructive re-entry conditions. AIAA AVIATION, 46th AIAA Thermophysics Conference, 2016, https://doi.org/10.2514/6.2016-4154. Paper AIAA-2016-4154.

[47] Y. Prevereaud, J.-L. Verant, M. Balat-Pichelin, J.-M. Moschetta, Numerical and experimental study of the thermal degradation process during the atmospheric re-entry of a tial6v4 tank, Acta Astronaut. 122 (2016) 258–286, https://doi.org/10.1016/j.actaastro.2016.02.009. http://www.sciencedirect.com/science/article/pii/S0094576516000564.